POLITECNICO DI TORINO
Repository ISTITUZIONALE

Efficient prediction of urban air mobility noise in a vertiport environment

Original
Efficient prediction of urban air mobility noise in a vertiport environment / Yunus, Furkat; Casalino, Damiano; Avallone, Francesco; Ragni, Daniele. - In: AEROSPACE SCIENCE AND TECHNOLOGY. - ISSN 1270-9638. - ELETTRONICO. - 139:(2023), p. 108410. [10.1016/j.ast.2023.108410]

Availability:
This version is available at: 11583/2978683 since: 2023-05-22T15:35:48Z

Publisher:
Elsevier

Published
DOI:10.1016/j.ast.2023.108410

Terms of use:

This article is made available under terms and conditions as specified in the corresponding bibliographic description in the repository

Publisher copyright
Elsevier postprint/Author's Accepted Manuscript

© 2023. This manuscript version is made available under the CC-BY-NC-ND 4.0 license http://creativecommons.org/licenses/by-nc-nd/4.0/.The final authenticated version is available online at: http://dx.doi.org/10.1016/j.ast.2023.108410

(Article begins on next page)

12 October 2024

Contents lists available at ScienceDirect

Aerospace Science and Technology

journal homepage: www.elsevier.com/locate/aescte

Efficient prediction of urban air mobility noise in a vertiport environment

Furkat Yunus [a,*], Damiano Casalino [a], Francesco Avallone [b], Daniele Ragni [a]

[a] Flow Physics and Technology Department, Delft University of Technology, Delft 2629HS, the Netherlands
[b] Department of Mechanical and Aerospace Engineering, Politecnico di Torino, 10129, Torino, Italy

ARTICLE INFO

Article history:
Received 7 December 2022
Received in revised form 15 May 2023
Accepted 16 May 2023
Available online xxxx
Communicated by Qiulin Qu

Keywords:
Urban air mobility
Gaussian beam tracing
Vertiport noise
Noise footprint
Wind effect

ABSTRACT

Efficient calculation of urban air mobility noise footprint in a vertiport environment, considering acoustic effects of various designs, operational conditions, and environmental factors, is essential to limit the noise impact on the community at an early stage. To this purpose, the computationally efficient low-fidelity approach presented by the authors in Fuerkaiti et al. (2022) [11] is extended to calculate the noise footprint of an aircraft in a generic 3D environment. The straight-ray propagator is replaced with a Gaussian beam tracer that accounts for complex source directivity, 3D varying terrain topology, and wind profiles. The reliability of the Gaussian beam tracer has been verified in previous studies by the authors. In this work, it is further extended to include complex source directivity in the presence of a moving medium. Noise sources, obtained using a low-fidelity toolchain, are stored on a sphere surrounding the aircraft and are propagated through an inhomogeneous anisotropic atmosphere. Noise footprints, predicted for different terrain topologies, source directivities, and wind flow conditions, are compared. It is shown that, compared to flat terrain, for the case under investigation, the building blocks increase on-ground noise levels by 5 dB in the illuminated zone due to multiple reflections; they also shield the incoming sound field by creating shadow zones behind the building. The shielding increases with increasing frequency in a quiescent atmosphere. The change between the source directivities, corresponding to the first and second harmonics of the blade passing frequency, results in a difference of up to 40 dB in the noise footprint. The presence of the wind flow can contribute a significant variation in the acoustic footprint by changing the lobes of the footprint pattern and intensifying the noise levels; the variation increases with increasing frequency. Compared to the straight-ray propagator, the present approach reduces the prediction error by 5 dB in the illuminated zones and 35 dB in the terrain shadow zones.

© 2023 The Author(s). Published by Elsevier Masson SAS. This is an open access article under the CC BY license (http://creativecommons.org/licenses/by/4.0/).

1. Introduction

Urban air mobility (UAM) vehicles, such as electric vertical takeoff and landing (eVTOL) aircraft powered by propellers, are expected to revolutionize transportation by extending it into three-dimension. These vehicles are expected to be adapted for low-altitude, short missions within a metropolitan area to connect residential locations and airports to city centers through vertiports. The vertiports are defined as nodes at the end of airspace corridors which are identifiable ground or elevated areas used for the takeoff and landing of eVTOL aircraft [1]. Among others, the spatial location of vertiports plays a crucial role in safer, faster, and more economical commuting within an urban area [1–3]. According to a survey reported in [2], 28% of people prefers elevated vertiports installed on the building rooftops that could reduce nuisance due to the vertiport's high traffic density. 65% of people likes to have vertiports closer to transportation hubs in a city center due to economic reasons and efficiency in total travel time.

Implementing vertiports in a densely populated residential area will require detailed analyses of noise propagation. Nevertheless, as highlighted in a most recent review paper about vertiports [1], the UAM community noise is described as the most under-represented topic in scientific research, regulatory guidelines, and vertiport design proposals. It was further stated that none of the current scientific contributions provide a distinct analysis of how noise is distributed in a vertiport environment considering different vertiport layouts, locations, local weather effects, and eVTOL aircraft designs. This paper focuses on a methodology to evaluate eVTOL aircraft noise footprint in a vertiport environment considering different vertiport locations and realistic weather conditions.

* Corresponding author.
E-mail address: f.yunus@tudelft.nl (F. Yunus).

https://doi.org/10.1016/j.ast.2023.108410
1270-9638/© 2023 The Author(s). Published by Elsevier Masson SAS. This is an open access article under the CC BY license (http://creativecommons.org/licenses/by/4.0/).

UNCORRECTED PROOF

Accurate prediction of noise propagation in a vertiport environment is challenging as various wave phenomena, i.e., multiple reflections, diffraction, refraction, and propagation scenarios such as standing waves with large amplitude oscillations in narrow urban canyons and scattering by atmospheric turbulence, should be accounted for. Multiple reflections take place between different building blocks, and refraction occurs due to the vertical and horizontal variation in air temperature and wind velocity gradients. Furthermore, building blocks can shield high-frequency noise while low-frequency noise diffracts into the building shadow zone. Moreover, sound can be scattered by the atmospheric turbulence induced by the high-rise building blocks. The inclusion of turbulence effects requires another level of sophistication in the prediction models, which is not in the scope of the present study.

Noise-power-distance (NPD) data [4], that are specific to each aircraft, have been widely used to evaluate aircraft noise impact on the community. NPD estimates noise levels for a specific aircraft type, at a given flight condition, e.g., forward flight, and distance from the observer. However, the absence of a comprehensive UAM vehicle performance model, aircraft noise data, and particularly a propagation model capable of accounting for the aforementioned propagation scenarios hinders the application of existing NPD data in estimating the noise footprint of UAM vehicles in a vertiport environment. In the absence of NPD, the acoustic footprints of an aircraft for different flight trajectories and operating conditions can be evaluated with two different methods. The first one is a direct approach that directly applies high-fidelity CFD solvers to calculate the flow field around the vehicle, noise emissions, and the noise footprint [5]. The second one adopts a hybrid approach that evaluates aircraft noise footprints in three steps. In the first step, the flow field around the vehicle is obtained by CFD simulation. In the second step, noise sources are sampled over a sphere/hemisphere surrounding the aircraft by means of the Ffowcs Williams & Hawkings (FW-H) acoustic analogy. In the third step, the noise signals are propagated from the noise sphere toward the ground using wave-based methods that solve the convected wave-equation using finite element method (FEM) [6], ray-tracing [7,8], or beam-tracing techniques [9,10]. The direct approach is restricted to relatively low-frequency and short-range propagation problems as it is computationally demanding and could be unaffordable when the acoustic impact of high-frequency noise or large propagation distances are considered. In the hybrid approach, the main computational limitation comes from the calculation of noise spheres, as high-fidelity CFD simulations are used. Nevertheless, high-fidelity CFD simulations are too expensive to design and evaluate low-noise aircraft and flight mission profiles that involve evaluating thousands of noise spheres, each one for a different combination of flight status parameters. Therefore, they cannot be coupled with a design optimization process to explore the acoustic effects of various environmental and operational parameters on the noise footprints in an industrial context.

Recently, the authors [11] developed a computationally efficient low-fidelity approach to calculate the noise footprint of propeller-driven aircraft and evaluate the acoustic effects of various design and operating parameters on the noise footprint. Their low-fidelity approach included tonal noise due to the volume displacement and the steady loading on the propeller blades, and the broadband contribution of trailing-edge boundary layer thickness noise. However, their work was limited to noise propagation in a quiescent, constant-temperature atmosphere over flat terrain, as the acoustic propagation is modeled with a straight ray tracing (SRT) model. The SRT model relies on source-receiver geometry and does not allow to account for atmospheric refraction due to variations in the weather conditions and multiple reflections over irregular terrain [8]. Barbarino et al. [12] developed a mixed-fidelity approach that consists of a low-fidelity and a high-fidelity approach. The former adapts a low-fidelity source noise model and a SRT model when the eVTOL is far from the urban center. The latter solves the acoustic scattering problem in the vicinity of an urban area by coupling FW-H approach with an acoustic solver based on the boundary element method (BEM) accelerated with a fast multipole technique. Nevertheless, the work did not investigate the atmospheric refraction effects due to 3D varying weather profiles in a city environment.

The authors [8] developed a two-point 3D eigenray tracer to include weather effects into the noise footprint. Their eigenray tracer accounts for sound refraction due to the vertical variability of air temperature and wind velocity gradients. Noise footprints were calculated on flat terrain, and the weather profiles were modeled using range-independent logarithmic wind and temperature profiles. Still, they did not address the acoustic effects of 3D varying terrain topology and wind flow distribution on acoustic propagation. Bian et al. [10] investigated drone noise impact using a low-fidelity approach and Gaussian beam tracing (GBT) model. They used an elementary source noise model [13], which does not account for blade geometry and load distribution along the blade span. A range-independent linear sound speed profile was employed to include refraction effects. However, in a realistic urban environment, temperature and wind velocity profiles are highly affected by urban canyons and become range-dependent. Thus, a linear range-independent sound speed profile can not approximate atmospheric refraction in a 3D urban environment [8]. Furthermore, their GBT model is restricted to an inhomogeneous isotropic atmosphere, hence, can not propagate noise signals in the presence of wind [9]. This restriction prevents the application of existing GBT models to include complex source directivity into the acoustic footprint in windy environments. This limitation is addressed through a novel approach in this study.

This paper presents a computationally efficient and robust methodology to investigate the acoustic impact of design, operating, and environmental parameters on the noise footprint of an aircraft in a generic 3D environment. To this end, the computationally efficient low-fidelity noise source prediction approach [11,14] is coupled with a GBT model developed by the lead author [15] that accounts for the acoustic effects of 3D varying terrain topology and wind profiles. The GBT model, in this work, is further extended to account for complex source directivity in the presence of atmospheric refraction due to variations in wind velocity distribution that constitutes another original contribution of the present work. The proposed approach aims to predict the noise footprints of an eVTOL vehicle in a vertiport environment. The study has a twofold objective: i) to compare the performance of the current GBT propagation model with the traditional SRT method in predicting noise footprints. ii) to evaluate the impact of terrain topology, source directivity, and wind flow distribution on the acoustic signature of an eVTOL aircraft during hover operations in a vertiport. The 3D wind profiles in the vertiport environment are directly imported from a high-fidelity CFD simulation. For this case study, the flow field is assumed not to affect the source noise sphere. Hence, the distance between the eVTOL and the surrounding buildings is considered to be larger than 40 times the rotor diameter.

The remainder of this paper is structured as follows. In Section 2, the numerical approach is described. In Section 3, verification results are presented. In Section 4, improvements in the footprint predictions, the acoustic effects of varying terrain topology, source directivity, and wind flow profiles on the noise footprint are studied for a case study. Finally, the conclusion of the work is given in Section 5.

UNCORRECTED PROOF

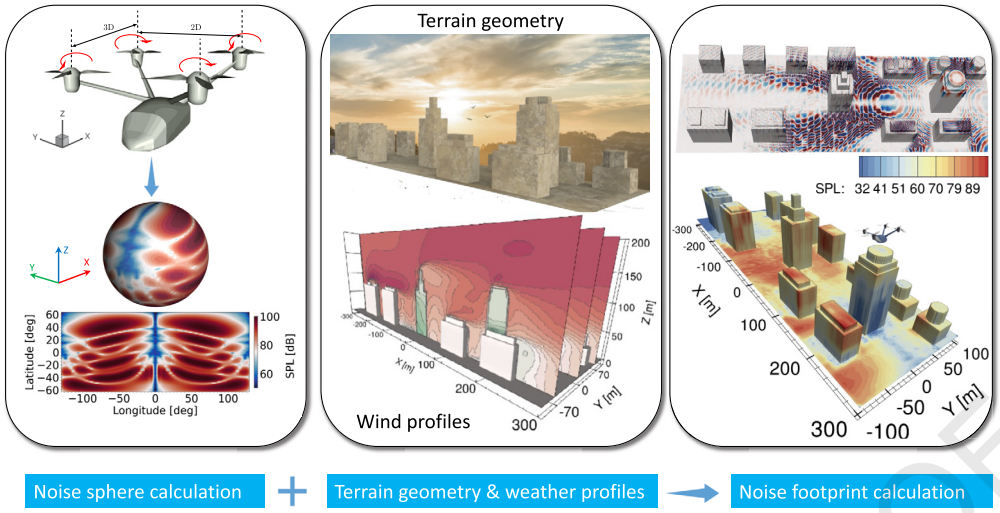

Fig. 1. Schematic illustration of the computational procedure. (For interpretation of the colors in the figure(s), the reader is referred to the web version of this article.)

2. Numerical approach

A standard hybrid approach is used to predict the source noise levels as well as the noise footprint of an eVTOL in a vertiport environment. Once the eVTOL geometry is given in terms of the blade, hub geometries, and relative positions between propellers, aerodynamic calculations, based on the blade element momentum theory (BEMT), are carried out with the *Opty∂B*-BEMT tool [14] to determine the radial distribution of aerodynamic loads and integral boundary layer parameters. The outputs of the BEMT calculation are used as inputs for a tonal and broadband aeroacoustic prediction tool *Opty∂B*-PNOISE. This tool calculates the noise signals on microphones distributed on a sphere surrounding the eVTOL vehicle. The tonal component contains thickness noise resulting from the volume displacement in the propeller rotation plane and loading noise due to steady loading on the propeller blades, respectively. The broadband component includes only the turbulent boundary layer trailing edge noise. The terrain geometry and 3D wind flow profiles are also provided as input. The 3D temperature and wind velocity profiles are modeled as a combination of 2D slices, as shown in Fig. 1. This approach allows for an efficient and effective representation of the 3D weather conditions in a given environment. After reading the noise sphere and environmental profiles, the eVTOL noise footprint is computed using a GBT-based propagation model [15]. The coupling of the low-fidelity noise source prediction method with the GBT-based propagation model presents a novel and efficient approach for evaluating the noise footprint of eVTOL aircraft in a vertiport environment. This innovative combination takes into account complex source directivity, 3D varying terrain geometry, and wind velocity profiles, providing a more accurate evaluation of noise impact. A schematic illustration of the computational procedure is displayed in Fig. 1.

2.1. Noise sphere calculation

The noise sphere calculation is carried out by employing the *Opty∂B*-BEMT and *Opty∂B*-PNOISE tools. *Opty∂B*-BEMT adopts a conventional BEMT formulation with uniform inflow and Prandtl tip-loss correction for loads computation. The aerodynamic module implemented inside the tool is based on the coupled panel/boundary layer model by Drela & Giles [16]. More details of the formulation can be found in the work of Casalino et al. [14]. The *Opty∂B*-PNOISE tool is used to calculate the noise signals on microphones distributed on a sphere surrounding the eVTOL. The tonal noise contribution is computed using either the time-domain FW-H formulation based on the compact dipole/monopole formulation by Casalino et al. [6] or the frequency-domain formulation derived by Hanson [17]. The frequency-domain formulation provides similar accuracy as the time-domain formulation while reducing the computational cost significantly [11]. The broadband noise contribution is computed using Roger and Moreau's trailing edge noise model extended to a rotating blade and by using the Schinkler and Amiet wall pressure spectrum model [18].

2.2. GBT-based noise footprint prediction

The GBT solver UYGUR (acoustic ray and Gaussian beam tracer) [15] is developed based on the 3D ray path tracing (RPT) method [19], and the GBT method [20] that accounts for multiple reflections over irregular terrain topology and atmospheric refraction due to vertical and horizontal variations in air temperature and wind velocity gradients. After reading as input the noise sphere and the environmental profiles, the noise levels at a receiver point are calculated in the following three steps. In the first step, rays are traced from the aircraft center position toward the ground, and ray-path trajectories are obtained by performing RPT. Next, the geometrical spreading and wavefront variation along each ray-path trajectory are determined by solving the dynamic ray tracing (DRT) equations [20]. The DRT equations allow for computing the travel time on the ray-path trajectories and their vicinity. The Gaussian beams are constructed along each ray-path trajectory based on the solution of RPT and DRT systems. Finally, the acoustic field at a receiver point is calculated by summing the contribution of each Gaussian beam passing nearby the receiver location.

UYGUR assumes an omnidirectional point source in which the beam strength is identical in all directions, i.e., all beams have the same initial phase and magnitude. This limitation does not allow the solver to simulate noise footprints of acoustic sources with complex source directivity. The present work extends UYGUR to include the complex source directivity into the acoustic footprint, which is achieved in the following two steps. The first step determines ray-sphere intersection points within the RPT procedure. Afterward, each Gaussian beam's initial phase and magnitude are updated with the ones stored on the ray-sphere intersection point and propagated towards the terrain with the DRT procedure. If no values are available at the intersection point, an interpolation based on the inverse-distance interpolation scheme is performed to determine the corresponding values using the data points available on the sphere. Compared to earlier works [9,10], the present

UNCORRECTED PROOF

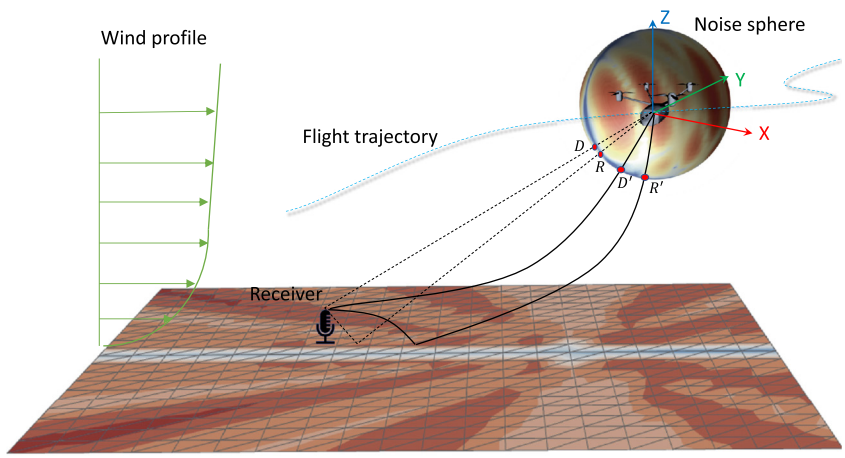

Fig. 2. A sketch of the source noise sphere and sound rays passing nearby a ground receiver. Dashed lines represent sound rays in a quiescent, homogeneous atmosphere, while curved solid lines represent the sound rays in a windy atmosphere.

approach has two remarkable advantages. First, it does not require modifying the beam summation equation, which removes extra computational time. Second, because of the anisotropic nature of the RPT and the DRT systems, the present GBT propagator can accurately propagate the noise signals even in the presence of strong refraction due to horizontal and vertical variations in air temperature and wind velocity gradients. In this case, sound rays curve more with increasing propagation distances resulting in the shift of the ray-sphere intersection points, as illustrated in Fig. 2. For instance, the ray-sphere intersection points corresponding to direct and ground reflected rays passing nearby the receiver location are shifted from D and R to D' and R', respectively, in the presence of wind. Furthermore, the present approach does not need to trace eigenrays connecting the source to the receivers by optimizing the shooting angles as presented in [8]. Instead, on-ground noise levels are calculated by weighted summation of contributions of each beam passing nearby the receiver location.

The shift in the ray-sphere intersection point will be evident on the noise footprint only if the source directivity pattern is well captured on the sphere with proper spatial resolution. In other words, the footprint accuracy highly depends on the spatial resolution of the noise sphere; a higher number of sampling points on the sphere usually gives much better accuracy but increases computational cost. This aspect will be investigated in the following section.

3. Validation and verification

The low-fidelity noise-sphere calculation toolchain composed of the *Opty∂B*-BEMT and *Opty∂B*-PNOISE tools was validated for a variety of propellers by comparing against experimental measurements [14] and high-fidelity simulations [14,11]. In addition, the GBT model was also verified by comparing it against an exact solution that describes the propagation of sound from a monopole source in a homogeneous isotropic atmosphere over flat terrain [8] and finite element solutions of the convected wave equation in the presence of multiple building blocks and 3D wind flow profiles [15].

This section first evaluates the accuracy of the noise sphere for a range of spatial resolutions. Then, the reliability of the present GBT tool to include complex source directivity into the acoustic footprint is assessed by comparing the noise footprints over flat terrain calculated with the GBT tool against a reference solution. The *Opty∂B*-FOOTPRINT [11] tool, based on the SRT model, is used as a reference solver. The reference solver follows NPD method for straight-line sound propagation in a homogeneous and still atmosphere over flat terrain, hence, can provide a 'true' answer for the validation case. *Opty∂B*-FOOTPRINT evaluates the noise levels at a receiver point by calculating the Euclidean distance between the source and the receiver and applying spherical spreading, atmospheric absorption according to SAE ARP866A, Doppler shift, and amplitude corrections related to the sphere radius and ground reflection. The SRT model allows only for a single reflection by mirroring the source with respect to the ground plane [7,8,11]. All tools run on an Intel(R) Xeon(R) Gold 6140 CPU @2.3 GHz processor with 36 cores.

3.1. The spatial resolution of the noise sphere

The same propeller but with five blades and the same validation case as described in [11] is considered. Two propellers instead of a single propeller are employed to highlight better the interference pattern on the source sphere caused by the acoustic interaction. The two propellers were designed to be symmetrical with respect to the XZ-plane. To minimize the impact of aerodynamic interaction on the acoustics, the tip-to-tip distance between them was set to 1D [21,22], where D is the diameter of the propellers (D = 2.5 m). The configuration of the twin propellers is illustrated in Fig. 3(a). Both propellers rotate at 1900 RPM at an altitude of 2000 m and each generates 1500 N thrust. The phase angle between the propellers is 0°. The advance ratio is $J = 0.84$. The blade passing frequency (BPF) is 158.33 Hz. The radius of the noise sphere is set to $R_h = 10D$. The atmosphere is homogeneous and quiescent and has a constant temperature of 22 C°. As illustrated in Fig. 3(b), a straight-level flight trajectory is considered that spans from a starting point S $(-5, 0, 2)$ km to a terminal point T $(5, 0, 2)$ km and has a length of 10 km. The flight trajectory is oriented along the X-axis of the ground reference system. The flight direction points to the positive X-axis. Two on-ground microphones are considered to investigate the noise signature. The first microphone (Mic 1) is located at the center of the ground plane (0, 0, 3) m and the second microphone (Mic 2) is located at (0, -2500, 3) m as shown in Fig. 3(b).

The spatial resolution of a sphere can be represented by the number of vertices on its surface. This can be determined by the number of points along the sphere's radius. Given μ points along the sphere's radius, the number of vertices on the sphere can be calculated as $(\mu + 1)^2$. This simple relationship allows for a precise representation of the sphere's surface and the grid representation of its geometry. Six noise spheres corresponding to $\mu = [8, 18, 22, 32, 47, 60]$ are considered, where $\mu = 8$ represents the coarsest sphere and $\mu = 60$ indicates the finest one. The noise spheres for each value of μ are calculated using the *Opty∂B*-BEMT

UNCORRECTED PROOF

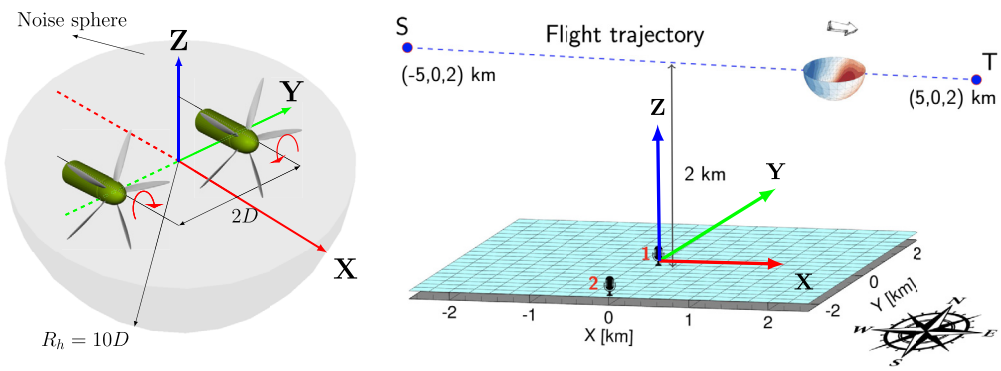

(a) Twin-propeller configuration. (b) The geometry of the problem and the reference system.

Fig. 3. A sketch of the twin-propeller configuration, the noise sphere and the reference system (a). The geometry of the problem (b), adapted from [11].

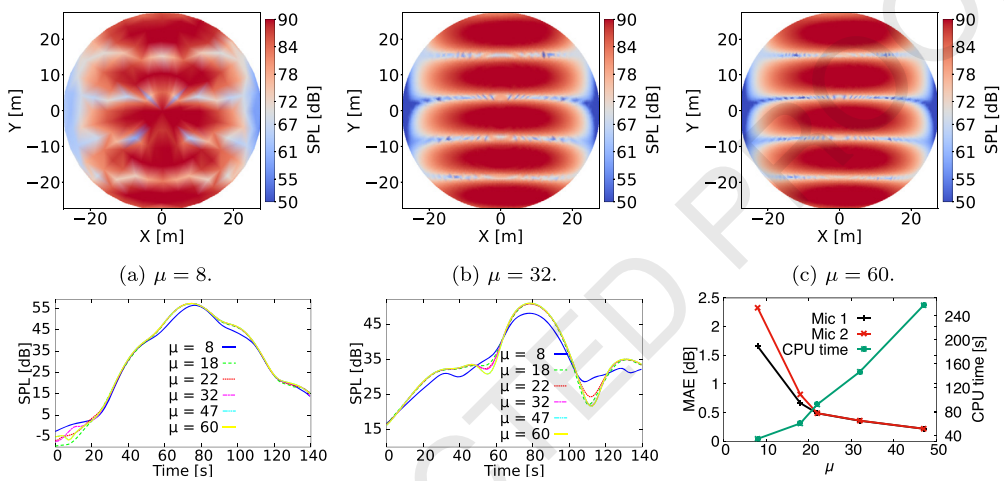

(a) $\mu = 8$. (b) $\mu = 32$. (c) $\mu = 60$.

(d) Mic 1. (e) Mic 2. (f) MAE and CPU time.

Fig. 4. Bottom view of the noise spheres of the twin-propeller configuration corresponding to $\mu = 8$ (a), $\mu = 32$ (b), and $\mu = 60$ (c). Noise signature at Mic 1(d) and Mic 2(e) and the MAE at Mic 1 and Mic 2 and CPU time as a function of μ (f).

and *Opty∂B*-PNOISE tools, and three of the noise spheres are displayed in Fig. 4. Due to the lower resolution of the noise sphere for $\mu = 8$, the interference dips and peaks are not well captured. However, a significant improvement is observed in the noise sphere for $\mu = 32$ as the separation between interference dips and peaks becomes more evident. At the same time, the noise spheres for $\mu = 32$ and $\mu = 60$ appear almost identical.

On-ground noise signatures of the six noise spheres at Mic 1 and Mic 2 are calculated using the reference solver and displayed in Fig. 4(d) and 4(e), respectively. At Mic 1, the difference between the noise signatures is not significant. The maximum difference between the noise signature for $\mu = 8$ and $\mu = 60$ is around 3 dB that appeared at flyover time $t = 7$ s. This slight difference is due to Mic 1 and the flight trajectory lying on the XZ plane. Hence, the ray-sphere intersection point on the noise sphere traverses within the same interference peak at the center of the bottom half of the noise sphere during the total flight time (see Fig. 4). At Mic 2, a significant change up to 8 dB is seen between the noise signature for $\mu = 8$ and $\mu = 60$. While the noise signatures for $\mu = 32$ and $\mu = 60$ remain nearly identical. This is attributed to the relative position of Mic 2 and the corresponding ray-sphere intersection point that crosses consecutive interference dips and peaks during the flyover time. To better highlight the accuracy of the noise sphere with respect to the different spatial resolutions, the mean absolute error (MAE) at Mic 1 and 2 are calculated for the five values of μ and plotted in Fig. 4(f). Here, the noise signature calculated with the larger μ is used as a reference. The noise signature calculated with a smaller μ is compared against the one computed with a subsequent larger μ. It is seen that for both microphones, the maximum MAE occurs for $\mu = 8$. The MAE is nearly identical at both microphone locations for $\mu \geq 32$ and is below 0.35 dB. Moreover, a two-fold reduction in the computation time is achieved for $\mu = 32$ with respect to $\mu = 47$. In the following, the spatial resolution of the noise sphere is set to $\mu = 32$.

3.2. Inclusion of complex source directivity into the acoustic footprint

The same validation case and the noise sphere calculated for $\mu = 32$ (see Fig. 4(b)), as outlined in the previous section, are considered. The source is stationary and located at (0,0,2000) m and the receivers are distributed over a 5 km square area at ground level. The noise footprints calculated with the GBT tool and the reference solver over the square area and on a line along the X-axis at Y = -2.4 km are compared and displayed in Fig. 5. In both results, the interference patterns on the source sphere are well captured on the noise footprints. A favorable agreement is observed between the two results that verifies the reliability of the present GBT-based propagation model for including complex source directivity into the acoustic footprint.

UNCORRECTED PROOF

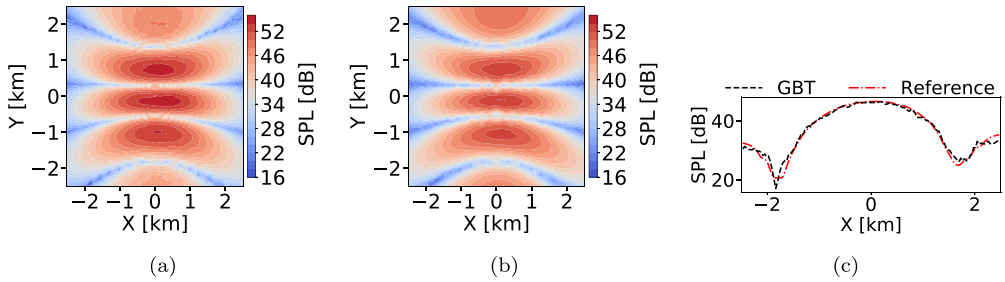

Fig. 5. Noise footprint computed with the GBT solver (a) and the reference (b) and comparison between them at a line along the X-axis at Y = -2.4 km (c).

4. Case study

4.1. Case setup

A quadrotor-like eVTOL vehicle is considered. The vehicle's gross weight is assumed to be 629 kg, which can carry a max of two people. The eVTOL is powered by four rotors, as shown in Fig. 6(a). The vehicle body is designed by the lead author based on the single-passenger quadrotor concept proposed by NASA [23], and delivered as part of a high-fidelity CFD simulation workflow for UAM noise research purposes [24]. For this case study, the vehicle body is for illustrative purposes only and is not used for the noise sphere calculation. Each rotor has three blades, and the blade has the same radial distribution of twist angle and chord length as the one described in [14]. The rotor diameter D is 1.8 m. In the local reference system of the vehicle, the relative distance between the two rotors along the Y-axis is set to $2D$ to avoid aerodynamic interference. At the same time, the distance between the rotors along the X-axis is set to $3D$. The rear rotors are elevated by $0.8D$ with respect to the front rotors to decrease the aerodynamic interaction between front, and rear rotors [25]. It is assumed that all four rotors rotate at the same rotational speed. Moreover, the total required thrust is distributed evenly at all rotors. Each rotor generates 1/4 of the target thrust, i.e., 1540 N, which is achieved by trimming the rotor blade pitch angle for a given rotor speed of 3000 RPM.

In this study, the source sphere radius was set to $13D$ to satisfy the acoustic far-field condition, which ensures that the acoustic field remains unaffected by the flow field. As the eVTOL fuselage does not significantly affect acoustics for this specific vehicle geometry [25], and the rotors are the primary noise source, noise scattered by the airframes is neglected. The noise spheres, corresponding to the first and second harmonics of the blade passing frequency (BPF) of 150 Hz, are computed using the *Opty∂B*-BEMT and *Opty∂B*-PNOISE tools. The acoustic pressure fluctuations at each microphone on the noise sphere are obtained by uncorrelated summation of the contribution of each rotor. The resulting acoustic spheres are plotted using the equidistant cylindrical projection [26] and displayed in Fig. 6(b) and Fig. 6(c), respectively.

The geometry of the vertiport and surrounding environment is modeled based on the recently released report by the Federal Aviation Administration (FAA) that provides guidance for vertiport design [3]. The report recommended the touchdown and lift-off area (TLOF) and final approach and takeoff area (FATO) to be elevated at least 0.8 m above the surrounding surface. The size of the TLOF, FATO, and safety area are characterized by square areas as illustrated in Fig. 7(a), which are measured based on an aircraft's controlling dimension (CD). The CD indicates the longest distance between the two farthest opposite points on the aircraft, e.g., rotor tip to rotor tip, measured on a level horizontal plane that includes all adjustable components extended to their maximum outboard deflection [3]. The width of TLOF is advised to be at least 1CD and the width of FATO to be 2CD, while the width of the safety area is recommended to be 3CD.

Table 1
Test matrix for the case study.

Case #	Solution method	f [Hz]	atmosphere	terrain
1	GBT	1th BPF	quiescent	non-flat
2	SRT	1th BPF	quiescent	non-flat
3	GBT	1th BPF	quiescent	flat
4	GBT	1th BPF	windy	non-flat
5	GBT	2nd BPF	quiescent	non-flat
6	GBT	2nd BPF	windy	non-flat

Based on the geometry of the eVTOL, whose CD equals $6D$, the safety area of the vertiport considered in this study is set to 3CD. Two different vertiport configurations are considered. The first one is an elevated vertiport installed on the rooftop of a high-rise building, and the building height is 12CD. This vertiport environment represents a typical city center connected with many transportation hubs. The eVTOL vehicle is hovering at an altitude of 19CD over the vertiport, as shown in Fig. 7(b). As the present GBT propagator does not account for diffracted wavefields behind the building blocks, the characteristic length of the smallest building is set to be 1.75 times larger than the wavelength of the fundamental frequency (first BPF) to minimize the diffraction effects. The second one is a ground-based vertiport installed on flat terrain, which shares the same ground area, and dimensions as the first vertiport environment, except for the vertiport location.

Two different atmospheric conditions are considered: a windy atmosphere and a quiescent atmosphere with a constant temperature of 22 C°. The mean flow in the metropolitan area is resolved using the high-fidelity CFD solver SIMULIA PowerFLOW®for an initial wind velocity of 5 m/s along the positive X-axis direction. Snapshots of the mean flow on the XY-plane at Z = 55 m and on the XZ-plane at Y = 0 m are displayed in Fig. 7(c) and Fig. 7(d), respectively. They show how the building geometries affect the wind field.

Altogether, 6 cases are considered to investigate differences in the footprint predictions with the GBT and SRT models, acoustic effects of varying terrain geometry, complex source directivity, and wind flow. The test matrix for this analysis is listed in Table 1. All Cases run on an Intel(R) Xeon(R) Gold 6140 CPU @2.3 GHz processor with 36 cores. To further highlight the difference between cases, noise levels at four particular regions, i.e., A, B, C, D, as indicated in Fig. 7(b), are considered.

4.2. Results

4.2.1. Improvements in the footprint prediction

The improvement in the footprint predictions is investigated by comparing the noise footprints calculated for Case 1 and Case 2. As shown in Fig. 8, in Case 2, the noise levels in the illuminated zones are predicted to be slightly lower than in Case 1, and the difference between the two cases varies in a range of 0-5 dB.

UNCORRECTED PROOF

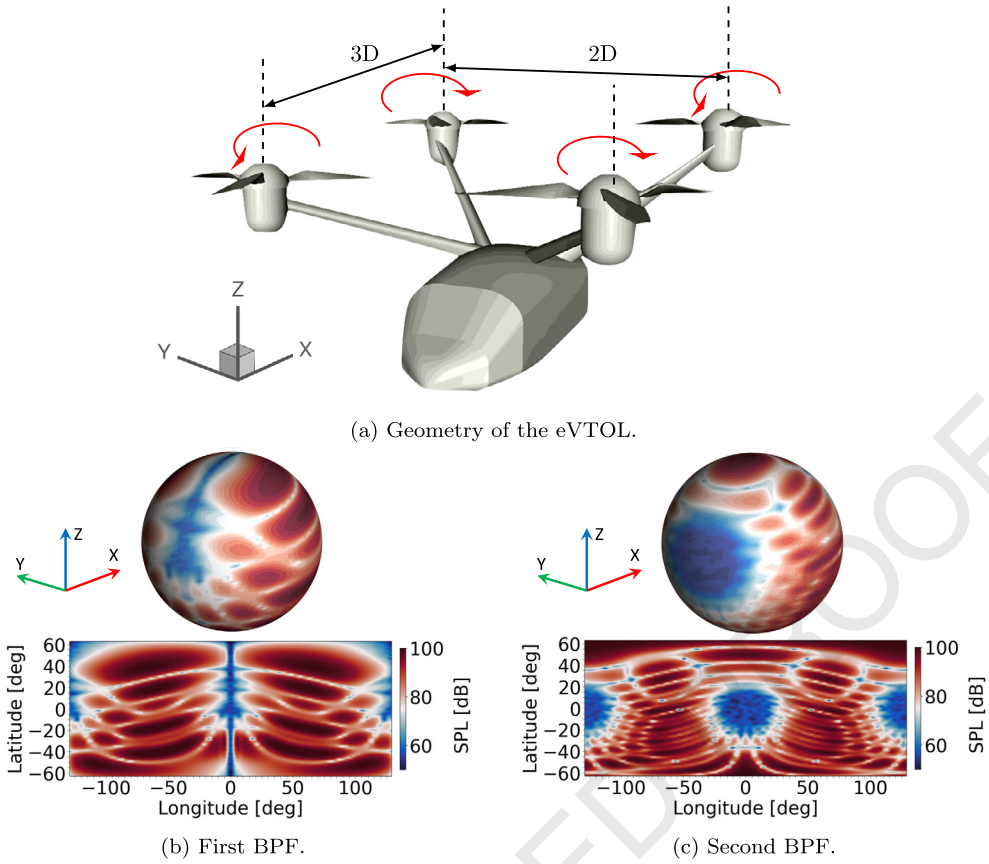

(a) Geometry of the eVTOL.

(b) First BPF. (c) Second BPF.

Fig. 6. The geometry of the eVTOL vehicle's four propellers, and the reference system (a). SPL computed over the noise sphere for the first BPF (150 Hz) (b) and the second BPF (300 Hz) (c).

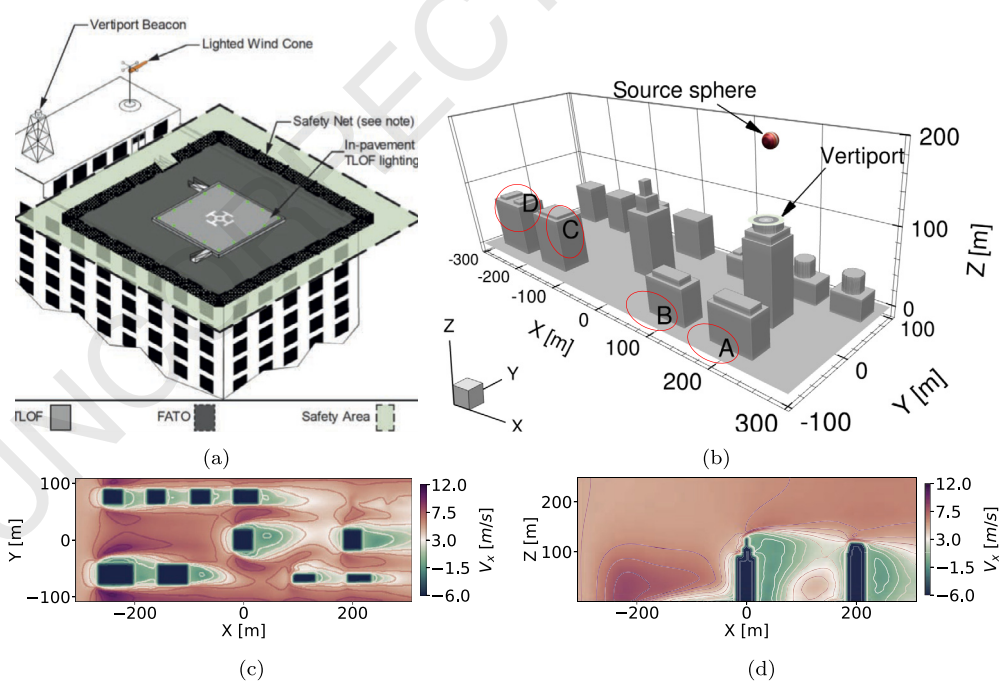

(a) (b)

(c) (d)

Fig. 7. An example of an elevated vertiport configuration [3] (a). An illustration of the urban environment includes an elevated vertiport (b). Snapshots of wind field on the XY-plane at $Z = 55$ m (c) and on the XZ-plane at $Y = 0$ m (d). The wind direction points to the positive X-axis.

This is attributed to the limitation of the SRT to include multiple reflections. The SRT model allows only for a single reflection, whereas the GBT can account for multiple reflections. A significant improvement noticed in the GBT solutions is the detection of irregular terrain surfaces and the proper prediction of terrain shadow zones. As seen, the SRT failed to predict the terrain shadow zones where the difference between the two solutions exceeds 35 dB. This is one of the main limitations of the SRT, which does not ac-

UNCORRECTED PROOF

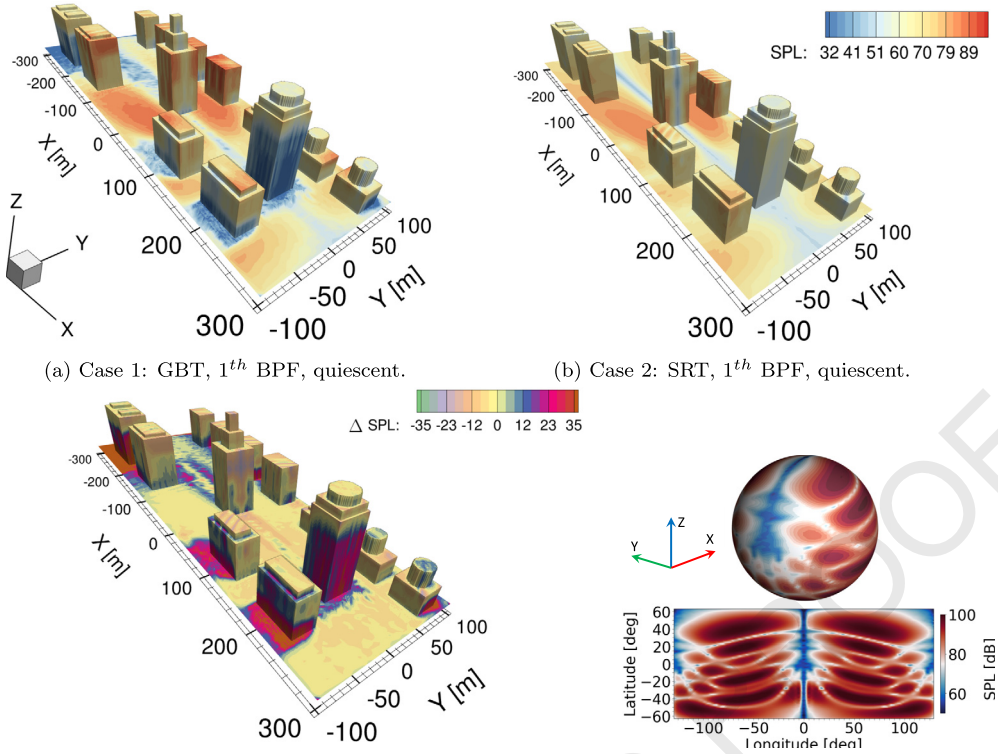

(a) Case 1: GBT, 1th BPF, quiescent.

(b) Case 2: SRT, 1th BPF, quiescent.

(c) $\Delta = (b) - (a)$.

(d) Noise sphere.

Fig. 8. Noise footprint of the eVTOL calculated with the GBT method (a) and the SRT method (b), the field difference between them (c) and the corresponding noise sphere (d) for the first BPF.

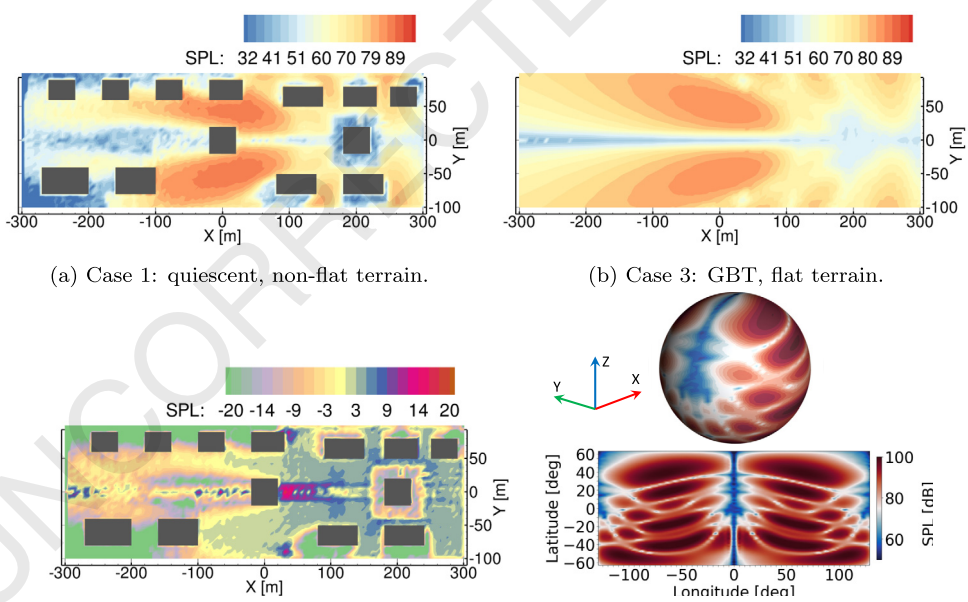

(a) Case 1: quiescent, non-flat terrain.

(b) Case 3: GBT, flat terrain.

(c) $\Delta = (b) - (a)$.

(d) Noise sphere.

Fig. 9. Noise footprint of the eVTOL in the urban area (a) and in flat terrain (b), the field difference between them (c) and the corresponding noise sphere (d) for the first BPF.

count for reflecting rays bouncing from the surfaces of obstacles. Additionally, it has been noted that the computational time of the SRT model is 3.7 s which is 15 times faster than the GBT approach (55.7 s).

4.2.2. Varying terrain geometry

The impact of varying terrain topology on the noise footprint is analyzed by comparing the results from Case 1 and Case 3. As shown in Fig. 9, the presence of building blocks leads to the creation of shadow zones due to the shielding of noise. Additionally, the building blocks result in multiple reflections that enhance noise levels in illuminated zones. In the illuminated zones of the urban area, the difference between the noise footprints varies between 0 dB and 5 dB due to the contribution of multiple reflecting rays. The maximum difference between the noise footprints is mainly distributed on the terrain shadow zones, where the dif-

UNCORRECTED PROOF

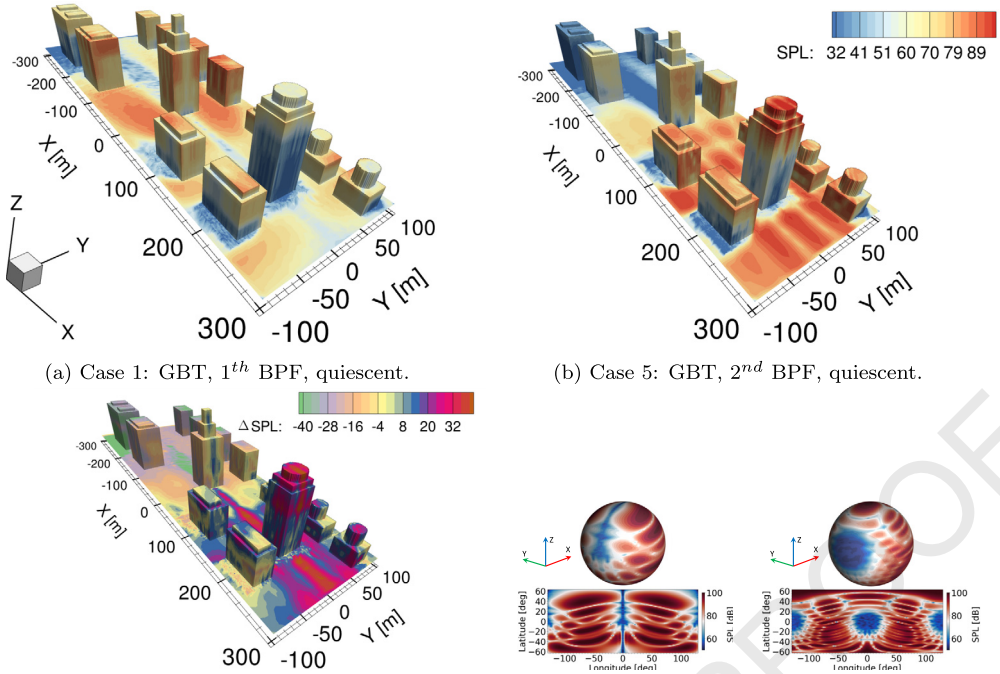

(a) Case 1: GBT, 1th BPF, quiescent.

(b) Case 5: GBT, 2nd BPF, quiescent.

(c) $\Delta = (b) - (a)$.

(d) 1th BPF.

(e) 2th BPF.

Fig. 10. Noise footprint of the eVTOL in the first BPF (a) and in the second BPF (b) and the field difference between them (c). The noise spheres for the first BPF (d) and the second BPF (e).

ference is more than 20 dB. The present GBT method does not account for the diffracted wavefield behind the building blocks. In reality, considering the diffracted wavefield in the terrain shadow zones, the difference would be different than 20 dB depending on the source frequency and characteristic length of the buildings. In Case 3, the computation time is 46.6 s, which is considerably lower compared to Case 1. This reduction in computation time is attributed to the fact that Case 3 only considered flat terrain and did not take into account multiple reflected rays between the building blocks.

4.2.3. Varying source directivity

The acoustic impact of varying source directivity on the noise footprint is examined by comparing the noise footprint calculated for Case 1 and Case 5. As shown in Fig. 10, the noise footprint on the illuminated zone shows a totally different pattern, and the varying source directivity contributes to a mismatch of up to 40 dB. Notably, the noise levels on the vertiport are increased up to 30 dB in Case 5 with respect to Case 1. Furthermore, in Case 5, the noise levels in the terrain shadow zones, particularly at regions A and B, are further decreased due to higher source frequency. This is expected physically and agrees with the results presented by several authors [27,28]; they reported that the diffraction shielding by the urban geometry is higher for the higher frequencies. Although the GBT method presented in this work does not account for the diffracted wavefield behind a building, the limiting ray, separating the illuminate and shadow zones, contributes to the shadow zone due to a finite beamwidth. This contribution is usually more substantial for lower frequencies than the higher ones as the beamwidth L is inversely proportional to the source frequency $L \propto \omega^{-1/2}$ [29]. As a consequence, a difference of up to 10 dB is seen in the terrain shadow regions A and B. Furthermore, it has been noted that the computational time (55.7 s) remains constant for both cases as the same spatial resolution is used for both noise spheres.

4.2.4. Varying atmospheric condition

The effects of varying wind conditions are evaluated for the first and second BPFs. For the first BPF, the noise footprints calculated for Case 1 and Case 4 are compared. As seen in Fig. 11, compared to Case 1, the on-ground noise levels in Case 4 increased considerably in the region enclosed by x = [-100, 300] m and y = [-100,-25] m, particularly behind the building at the center of the domain and region A and B. As outlined in the previous sections, those regions are seen as terrain shadow zones, and due to the presence of the wind flow, sound rays are refracted into those regions, eventually raising the noise levels. As highlighted in [8], the weather significantly impacts the predicted noise footprint at longer distances due to the refractive shadow zone that occurs when the source-receiver distance is a few times larger than the source height, and the local sound speed decreases towards the receiver. This is also observed in Fig. 11(b), where the noise levels drop significantly at the rooftop of the farthest buildings, particularly at region D. As shown in Fig. 11(c), the presence of the wind can contribute up to 23 dB difference in the predicted noise footprint, changing the lobes of the footprint pattern and intensifying the noise levels.

For the second BPF, the acoustic footprint calculated for Case 5 and Case 6 are compared. The wind effect becomes even more substantial than the one at the first BPF, as seen in Fig. 12. This is attributed to an increase in the source frequency. As outlined in the previous section, high-frequency noise is shielded by the urban topology, while lower-frequency noise diffracts into the building shadow region. In the presence of the wind field, the shielding is reduced due to atmospheric refraction, which mainly influences the higher frequencies [27]. Moreover, in the presence of the wind flow, the sound rays connecting the source to the receiver become more curved, particularly for distant receivers. Thus, the ray-sphere intersection points shift. Consequently, the noise signals propagated from the noise sphere toward distant receivers change accordingly. This can be seen from the sudden change of the noise levels predicted on the illuminated surface of the building in region C.

UNCORRECTED PROOF

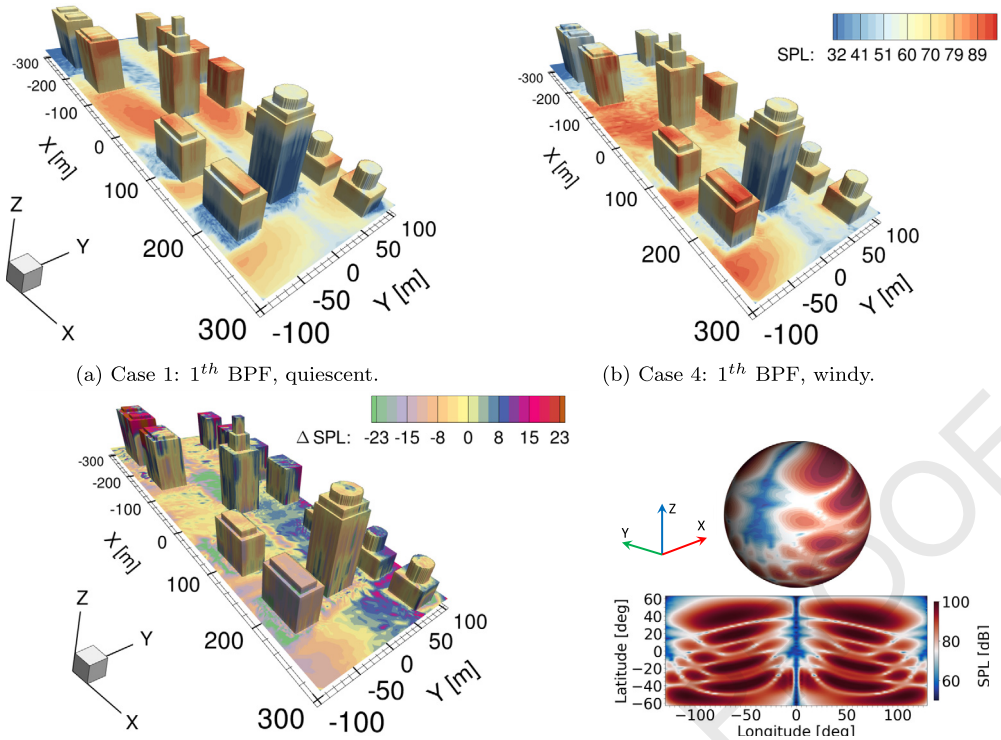

(a) Case 1: 1th BPF, quiescent.

(b) Case 4: 1th BPF, windy.

(c) $\Delta = (a) - (b)$.

(d) Noise sphere.

Fig. 11. Noise footprint of the eVTOL in a quiescent atmosphere (a) and in a moving inhomogeneous atmosphere (b), the field difference between them (c) and the corresponding noise sphere (d) for the first BPF.

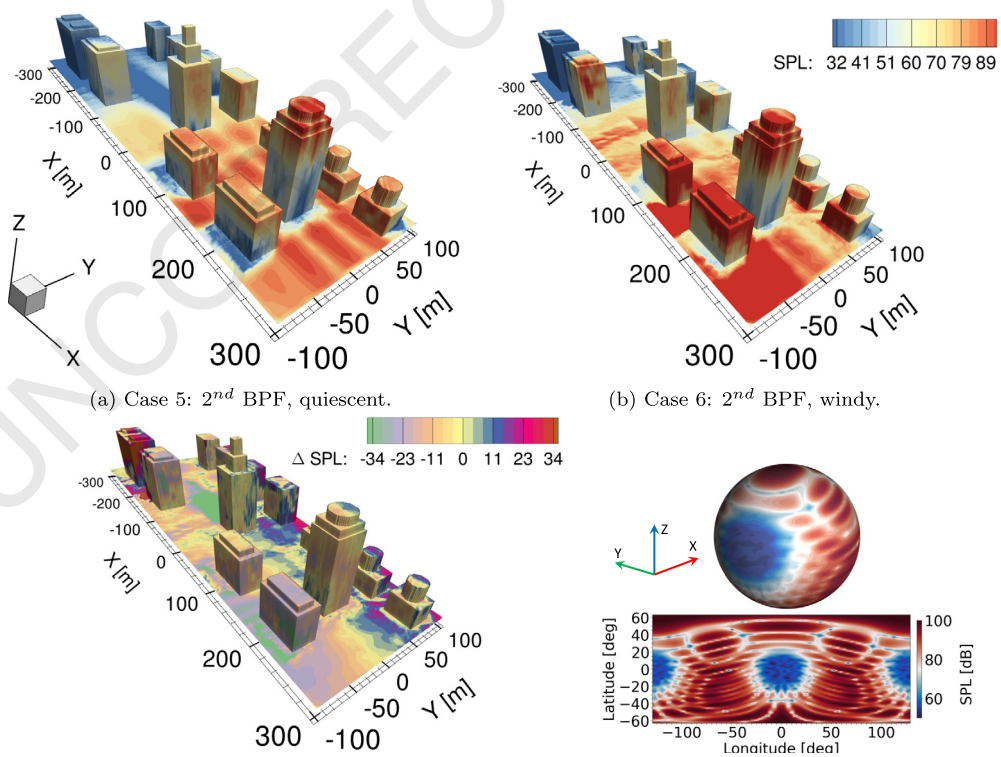

(a) Case 5: 2nd BPF, quiescent.

(b) Case 6: 2nd BPF, windy.

(c) $\Delta = (a) - (b)$.

(d) Noise sphere.

Fig. 12. Noise footprint of the eVTOL in a quiescent atmosphere (a) and in a moving inhomogeneous atmosphere (b), the field difference between them (c) and the corresponding noise sphere (d) for the second BPF.

UNCORRECTED PROOF

Generally, a significant difference in the predicted footprints with and without wind flow can be expected, particularly in the terrain shadow regions (regions A and B) and refractive shadow regions (regions C and D). The present results are in close agreement with the findings of a previous work [27], which showed that the wind effect might reach over 30 dB for a single 1/3 octave band and ranges from 15 to 23 dB(A) for road traffic noise propagating across multiple urban canyons. Nevertheless, in a more realistic scenario considering the effects of diffraction and atmospheric turbulence, the difference would be smaller than 23 dB. Moreover, it is observed that the computation time increases by twofold (122.5 s) in Cases 4 and 6, in which wind flow is considered. This is attributed to the additional computation required for interpolating weather data at each step of the ray propagation.

5. Conclusion

A new computational framework that couples computationally efficient methods, which were initially validated against high-fidelity simulation results, is presented to predict the noise footprint of an eVTOL vehicle hovering in a vertiport environment. The SRT model is replaced with the more advanced propagation model, based on the GBT method, that accounts for sound wave refraction, and multiple reflections due to 3D variations in the weather conditions and terrain topology. The GBT model is further extended to include complex source directivity with a novel numerical approach without modifying the beam summation equation and without tracing eigenrays. The reliability of the outline approach to include the complex source directivity is verified. The computational framework is then applied to investigate the acoustic effects of 3D wind flow distribution and terrain topology on the noise footprint of an eVTOL aircraft hovering in a vertiport environment. For the case under investigation, it is found that the building blocks increase on-ground noise levels by 5 dB in the illuminated zone due to multiple reflections and shield the incoming sound field by creating shadow zones behind the building. The effectiveness of noise shielding increases with increasing frequency in a quiescent atmosphere. The variation in the source directivity results in a difference of up to 40 dB in the noise footprint. The presence of the wind flow can contribute a significant variation in the acoustic footprint by changing the lobes of the footprint pattern and intensifying the noise levels; the variation increases with increasing frequency. The presented approach shows differences up to 35 dB in the terrain shadow zones and 5 dB in the illuminated zones with respect to the SRT-based noise footprint prediction approach. It is noticed that the computation time increases as the complexity of the propagation environment increases.

The results suggest that in the presence of irregular terrain surfaces, methods like GBT must be employed to account for multiple reflections over terrain surfaces and terrain shadow zones. Due to the low-operational altitude, the high-frequency noise from the UAM vehicles may not be masked by the background noise [30,31], cannot be properly shielded by the building blocks due to wind flow effects, and could impact the community. Thus, high-frequency noise should be among the main targets to mitigate UAM noise in a vertiport environment.

This study offers new insights into the potential of the GBT propagation model for predicting eVTOL noise footprints. However, it is important to acknowledge the limitations of this study. The GBT method used in this study does not account for diffracted wavefields behind buildings and the impact of atmospheric turbulence on sound propagation. To improve noise modeling in urban environments, diffracted wavefields should be included, and advanced models should be used to account for atmospheric turbulence effects. It should be noted that while it is impossible to validate the presented approach against measurement data on the urban scale, it can be validated against scaled urban models if measurement data from such models is available.

Declaration of competing interest

The authors declare that they have no known competing financial interests or personal relationships that could have appeared to influence the work reported in this paper.

Data availability

No data was used for the research described in the article.

Acknowledgements

This work has been financially supported by Airbus Defense and Space GmbH.

References

[1] K. Schweiger, L. Preis, Urban air mobility: systematic review of scientific publications and regulations for vertiport design and operations, Drones 6 (7) (2022) 179.
[2] E. Çetin, A. Cano, R. Deransy, S. Tres, C. Barrado, Implementing mitigations for improving societal acceptance of urban air mobility, Drones 6 (2) (2022) 28.
[3] Federal Aviation Administration (FAA), Memorandum subject to Engineering Brief No. 105, vertiport design, https://www.faa.gov/airports/engineering/engineering_briefs/drafts/media/eb-105-vertiport-design-industry-draft.pdf. (Accessed 17 October 2022).
[4] ECAC, Doc. 29, Report on Standard Method of Computing Noise Contours Around Civil Airports. Volume 2: Technical Guide, 4th ed., Tech. Rep., European Civil Aviation Conference, Neuilly-sur-Seine, France, 2016.
[5] D. Casalino, W.C. van der Velden, G. Romani, I. Gonzalez-Martino, Aeroacoustic analysis of urban air operations using the LB/VLES method, in: 25th AIAA/CEAS Aeroacoustics Conference, 2019, p. 2662.
[6] D. Casalino, M. Barbarino, A. Visingardi, Simulation of helicopter community noise in complex urban geometry, AIAA J. 49 (8) (2011) 1614–1624.
[7] D. Casalino, W.C. van der Velden, G. Romani, Community noise of urban air transportation vehicles, in: AIAA Scitech 2019 Forum, 2019, p. 1834.
[8] Y. Fuerkaiti, D. Casalino, F. Avallone, D. Ragni, Toward inclusion of atmospheric effects in the aircraft community noise predictions, J. Acoust. Soc. Am. 150 (2) (2021) 759–768.
[9] H. Bian, R. Fattah, S. Zhong, X. Zhang, On the efficient modeling of generic source directivity in Gaussian beam tracing, J. Acoust. Soc. Am. 149 (4) (2021) 2743–2751.
[10] H. Bian, Q. Tan, S. Zhong, X. Zhang, Assessment of uam and drone noise impact on the environment based on virtual flights, Aerosp. Sci. Technol. 118 (2021) 106996.
[11] Y. Fuerkaiti, E. Grande, D. Casalino, F. Avallone, D. Ragni, Efficient low-fidelity aeroacoustic permanence calculation of propellers, Aerosp. Sci. Technol. 123 (2022) 107438.
[12] M. Barbarino, F. Petrosino, A. Visingardi, A high-fidelity aeroacoustic simulation of a VTOL aircraft in an urban air mobility scenario, Aerosp. Sci. Technol. 125 (2022) 107104.
[13] D.B. Hanson, D.J. Parzych, Theory for noise of propellers in angular inflow with parametric studies and experimental verification, in: Final Report United Technologies Corp, 1993.
[14] D. Casalino, E. Grande, G. Romani, D. Ragni, F. Avallone, Definition of a benchmark for low Reynolds number propeller aeroacoustics, Aerosp. Sci. Technol. 113 (2021) 106707.
[15] F. Yunus, D. Casalino, F. Avallone, D. Ragni, Efficient prediction of airborne noise propagation in a non-turbulent urban environment using Gaussian beam tracing method, J. Acoust. Soc. Am. 153 (4) (2023) 2362.
[16] M. Drela, M. Giles, Viscous-inviscid analysis of transonic and low Reynolds number airfoils, AIAA J. 25 (1987) 1347–1355, https://doi.org/10.2514/3.9789.
[17] D.B. Hanson, Helicoidal surface theory for harmonic noise of propellers in the far field, AIAA J. 18 (10) (1980) 1213–1220.
[18] R. Schlinker, R. Amiet, Helicopter rotor trailing edge noise, in: 7th Aeroacoustics Conference, 1981, p. 2001.
[19] V.E. Ostashev, D.K. Wilson, Acoustics in Moving Inhomogeneous Media, 2nd edition, CRC Press, 2015.
[20] V. Červený, I. Pšenčík, Gaussian beams in inhomogeneous anisotropic layered structures, Geophys. J. Int. 180 (2) (2010) 798–812.
[21] T. Zhou, R. Fattah, Tonal noise acoustic interaction characteristics of multi-rotor vehicles, in: 23rd AIAA/CEAS Aeroacoustics Conference, 2017, p. 4054.

UNCORRECTED PROOF

[22] R. de Vries, N. van Arnhem, T. Sinnige, R. Vos, L.L. Veldhuis, Aerodynamic interaction between propellers of a distributed-propulsion system in forward flight, Aerosp. Sci. Technol. 118 (2021) 107009.
[23] W. Johnson, C. Silva, E. Solis, Concept vehicles for VTOL air taxi operations, in: AHS Specialists' Conference on Aeromechanics Design for Transformative Vertical Flight, No. ARC-E-DAA-TN50731, 2018.
[24] R. Atasi, I. Paden, Y. Fuerkaiti, I. Gonzalez-Martino, D. Casalino, C. Garcia-Sanchez, Numerical aerodynamics and aeroacoustics predictions of a drone under real urban environments, in: Quiet Drones Symposium 2022, 2022.
[25] Z. Jia, S. Lee, Acoustic analysis of a quadrotor eVTOL design via high-fidelity simulations, in: 25th AIAA/CEAS Aeroacoustics Conference, 2019, p. 2631.
[26] J.P. Snyder, Map Projections–a Working Manual, vol. 1395, US Government Printing Office, 1987.
[27] M. Hornikx, M. Dohmen, K. Conen, T. van Hooff, B. Blocken, The wind effect on sound propagation over urban areas: predictions for generic urban sections, Build. Environ. 144 (2018) 519–531.
[28] M. Hornikx, J. Forssén, Noise abatement schemes for shielded canyons, Appl. Acoust. 70 (2) (2009) 267–283.
[29] Y. Gabillet, H. Schroeder, G.A. Daigle, A. L'Espérance, Application of the Gaussian beam approach to sound propagation in the atmosphere: theory and experiments, J. Acoust. Soc. Am. 93 (6) (1993) 3105–3116.
[30] Z.H. Jia, S. Lee, Computational study on noise of urban air mobility quadrotor aircraft, J. Am. Helicopter Soc. 67 (1) (2022) 1–15.
[31] S. Lee, et al., Prediction of urban air mobility multirotor VTOL broadband noise using ucd-quietfly, J. Am. Helicopter Soc. 66 (3) (2021) 1–13.

UNCORRECTED PROOF